Slot-based Pattern Reconfigurable ESPAR Antenna for IoT Applications

Luca Santamaria, *Student Member, IEEE*, Fabien Ferrero, *Member, IEEE*, Robert Staraj, *Member, IEEE*, and Leonardo Lizzi, *Senior Member, IEEE*

***Abstract*— In this paper, a slot-based electronically steerable parasitic array radiator (ESPAR) antenna suitable for Internet-of-Things (IoT) applications is proposed. The antenna can provide 12 directive and 2 slightly different omnidirectional radiation states. The 12 directive patterns allow the antenna to focus the radiated energy towards 6 different directions uniformly distributed in the azimuth plane and with 2 different beamwidths. The reconfiguration of the radiation pattern is based on the use of low-capacitance low-power consuming diodes that can be digitally controlled. The paper details the design of the antenna structure and the practical implementation of the reconfiguration mechanism, discussing the effects of real electronic components on the antenna performance. The antenna effectiveness is numerically and experimentally assessed.**

***Index Terms*—ESPAR, pattern reconfigurable antenna, PIN diodes, Internet-of-Things (IoT).**

I. Introduction

The ongoing rapid growth of the Internet-of-Things (IoT) driven by applications such as smart city, smart home, and industry 4.0, will require billions of objects to be connected to the internet in the next future [1]. The huge traffic that will be generated by the communications between the objects and the network will pose demanding challenges in terms of reliability of the radio access [2] and reduction of the energy consumption [3]. On one hand, in fact, the huge number of communications will cause packet collisions that decrease the overall network performance. On the other hand, such collisions imply packet retransmissions, which increase the power consumption of the nodes despite their usually limited energy resources.

In this scenario, the use of pattern reconfigurable antennas (at the device and/or network side), which can steer the main beam towards a specific direction, can provide several advantages, such as a better spatial reuse, interference reduction and jamming suppression, fight of the multipath fading and improved coverage [4], [5]. In [6] it has been demonstrated that equipping the nodes of a sensor network with switched beam antennas can lead to 88% less energy used on average per packet transmission and 24% less data collisions.

Classical beam steering antennas like phased arrays, however, hardly fit the hard constraints typical of modern compact IoT devices. A more promising solution to form a desired antenna beam and to electronically control the associated direction of maximum radiation without the use of expensive phase shifters, high power consuming components, and within a limited form factor, is represented by the electronically steerable parasitic array radiators (ESPARs). Based on the theory proposed by Harrington [7], an ESPAR antenna is constituted by a single driven element surrounded by passive elements connected to reactive loads. The overall antenna radiation pattern is formed by combining the contributions of both the active and the passive radiating elements, these latter being excited through the coupling mechanism. The pattern reconfiguration can therefore be obtained by properly varying the reactance values.

In [7] both the driven and the parasitic elements were classical dipoles. Dipoles are good to perform theoretical studies [8], however they are difficult to be employed in practical applications due to the lack of a ground plane. Monopole-based ESPAR structures are certainly more convenient since they allow the integration with the beam-steering electronics and the feeding cable without affecting the antenna radiation characteristics [9]–[11]. On the other hand, the limited dimension of the ground plane tilts the maximum of radiation in the elevation plane [12], which is a problem in dealing with IoT applications where all the connected objects are supposed to communicate in the same horizontal plane. Such an issue can be solved by modifying the antenna ground plane with a metallic skirt wound around it, as done in [13]–[16]. More recently, an alternative solution based on dipoles has been proposed in [17]. In this case, a floating ground plane decoupled at the radio frequency (RF) has been used for the beam-steering electronics. Finally, in order to reduce the overall antenna height, the radiating elements can be folded [16], capacitively loaded [17] or embedded in a dielectric material [14].

In this paper, a new slot-based ESPAR antenna is proposed. The antenna can provide 12 directive pattern configurations and 2 slightly different omnidirectional states. The directive patterns are uniformly distributed and cover the entire azimuth plane. Whatever the pattern configuration, the maximum of radiation lies in the horizontal plane without any tilt in the elevation plane. The reconfiguration mechanism is based on the use of low-cost low-power switches that can be digitally controlled. All these characteristics make the proposed antenna a perfect candidate for modern IoT applications where spatial filtering is crucial to handle a massive number of connected objects.

A preliminary concept was proposed in [18]. However, the proposed antenna could provide a very limited number of radiation states (only 3) and the realization was not suitable for

Paper submitted on April 3, 2020.

All the authors are with Université Côte d'Azur, CNRS, LEAT, Sophia Antipolis, France (e-mail: leonardo.lizzi@univ-cotedazur.fr).

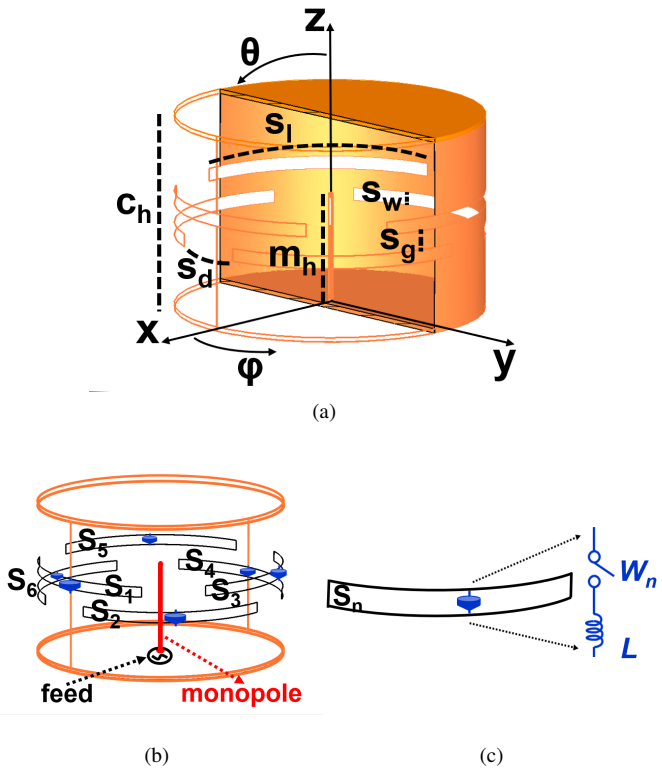

Figure 1. Proposed antenna structure: (a) geometrical parameters, (b) position of the 6 slots, and (c) reconfiguration circuit.

practical applications. However, the proposed antenna could provide only 3 radiation states (which makes it unsuitable for large scale IoT network applications), its spatial filtering capability and its capacity of attenuating the interference was limited, and the realization process was more appropriate for a proof-of-concept rather than a practical application. The antenna design has been therefore successively improved, increasing the number of radiation configurations and optimizing the radiation characteristics as shown by numerical results presented in [19]. This paper expands and complete the work in [19] explaining in detail the antenna design procedure, discussing the real implementation of the antenna and the reconfiguration mechanism and reporting the realization of the antenna prototype and its experimental assessment.

The rest of the paper is organized as follows. In Sect. II, the design of the antenna, including the description of the geometry, the optimization process and the resulting antenna performance, is detailed. Sect. III discusses the practical implementation of the reconfiguration mechanism, highlighting the effects of non-ideal electronic components. In Sect. IV, the effectiveness of the proposed design is evaluated through both numerical and experimental results. Finally, some conclusions are drawn in Sect. V.

II. Antenna Design

A. Antenna Structure

The proposed antenna structure (Fig. 1) consists of a metallic closed cylinder, whose height is indicated by c_h. On the lateral surface of the cylinder, 6 uniformly separated horizontal slots of dimension $s_l \times s_w$ are carved on 2 different levels, whose vertical separation is indicated by s_g. Each slot level is rotated by 60^o with respect to the other. The distance between two slots on the same level is indicated by s_d. The combination of s_l and s_d defines the cylinder circumference and consequently its diameter. The radius of the cylinder changes when s_d and s_l vary and the circumference of the antenna structure is therefore equal to $3s_d$+$3s_l$. The 3 lower slots are located at a height of $z = 18.25$ mm, while the 3 upper slots are located at $z = 25.75$ mm. The slots are named $S_n; n = 1, ...6$ with the normal to the n-tn slot being directed towards the direction at $\varphi = (n-1)60^o$ (Fig. 1(b)). A monopole of length m_l m_h is located at the center of the cylinder and fed through the bottom plate. The radius of the feeding monopole is 0.5 mm.

The structure can be considered as an ESPAR antenna where the parasitic radiating elements are the slots, while the driven one is the monopole. The working principle of the proposed antenna is that of an ESPAR antenna. In our solution, the driven element is the monopole at the center of the cylindrical cavity, while the passive elements are the slots.

In classical ESPAR antennas, the parasitic elements are base-loaded with varactor diodes whose voltage controlled reactances produce different antenna radiation patterns [20], [21]. Varactors diodes, however, are not suitable for IoT applications, because of their limitations in terms of power handling and voltage level required to control the varactor state. In the proposed antenna, in order to obtain a solution suitable for IoT applications, the reconfigurable circuit is constituted by a switch $W_n; n = 1, ...6$ in series with a fixed inductor L. The circuit is located at the center of each slot S_n connecting the two opposite sides (Fig. 1(c)). Such configuration allows only two possible impedance values to be put in parallel to each slot own impedance: $Z_o = \infty$ when the switch is open and $Z_c = j2\pi fL$, f being the working frequency, when the switch is closed. Having only two possible reconfiguration states at each slot, certainly limits the number of radiation pattern configurations that can be realized. However, this allows the antenna to be easily reconfigured using a low-power microcontroller, since each slot switch can be controlled by a 1-bit digital output.

The antenna total radiation pattern is the result of the combination of the field radiated by the driven monopole and those radiated by the parasitic slots. Switching between Z_o and Z_c modify the currents surrounding the slots, thus the fields they radiate and, consequently, the overall antenna radiation pattern. By properly selecting the value of the inductor L, and consequently of Z_c, the energy radiated by the monopole and the slots can be combined to obtain globally a directive radiation pattern.

B. Antenna Optimization

The antenna has been optimized by considering a reference configuration where only the switch W_1 (located on S_1) is open while all the others $W_n; n = 2, ...6$ are closed. Moreover, the switches are considered as ideal, i.e., they are modeled as an open circuit when they are open and as a short circuit when closed.

The antenna design procedure consists of two consecutive steps. The first one is aimed at optimizing only the antenna geometrical parameters, while the value of the inductors used in the reconfiguration circuits is set to $L = 0$ H. In the second step, the antenna structure is considered as fixed, and the inductance value L is optimized.

To obtain a solution suitable for IoT applications, the antenna is needed to fit the following electrical and radiating requirements. In terms of impedance matching, the antenna must exhibit

$$|S_{11}(f)| \leq S_{11}^T = -10 \text{ dB} \quad f_1 \leq f \leq f_2 \tag{1}$$

where $|S_{11}(f)|$ indicates the magnitude of the complex reflection coefficient in dB, $f_1 = 2.40$ GHz and $f_2 = 2.48$ GHz are the limits of the 2.4 WiFi frequency band, and the superscript T denotes the target value imposed by the project specification. This will ensure the minimization of the impedance mismatch losses and consequently the optimization of the available energy on the IoT device. In terms of radiation behavior, the antenna is required to have a good front-to-back ratio FB at the central frequency of the operating band, i.e.,

$$FB(f_c) \geq FB^T = 15 \text{ dB} \quad f_c = 2.44 \text{ GHz}. \tag{2}$$

FB is here calculated as the difference (in dB) between the gain in direction of maximum radiation φ^{mr} in the horizontal plane ($\theta = 90^o$) and the gain in the opposite direction ($\varphi^{mr} - 180^o, \theta = 90^o$). As shown in [6], having a good FB allows the antenna to filter the signals coming from undesired directions, thus drastically reducing the number of packet collisions and the overall energy consumption of the IoT network.

The optimization performed during the first design step is mathematically reformulated as the problem of identifying the optimal values $\hat{\mathbf{a}}$ of the antenna geometrical descriptors (see Fig. 1)

$$\mathbf{a} = \{s_l, s_w, s_g, s_d, c_h, m_h\} \tag{3}$$

that minimize a suitable cost function Ψ taking into account the above mentioned antenna requirements, i.e.,

$$\begin{aligned} \hat{\mathbf{a}} &= \underset{\mathbf{a}}{\text{argmin}}\{\Psi(\mathbf{a})\} \\ &= \underset{\mathbf{a}}{\text{argmin}}\{\alpha\Psi_{S_{11}}(\mathbf{a}) + \beta\Psi_{FB}(\mathbf{a})\}. \end{aligned} \tag{4}$$

In (4), $\Psi_{S_{11}}$ and Ψ_{FB} are the cost function terms associated to the impedance matching and radiation behavior requirements, respectively, and defined as

$$\Psi_{S_{11}} = \begin{cases} \frac{|S_{11}(f)| - S_{11}^T}{S_{11}^T} & \text{if } \Psi_{S_{11}} > 0 \\ 0 & \text{if } \Psi_{S_{11}} \leq 0 \end{cases} \tag{5}$$

and

$$\Psi_{FB} = \begin{cases} \frac{FB^T - FB(f_c)}{FB^T} & \text{if } \Psi_{FB} > 0 \\ 0 & \text{if } \Psi_{FB} \leq 0. \end{cases} \tag{6}$$

Finally, α and β are coefficients used to weigh the two cost function components. Since FB will be further enhanced through the correct choice of the inductors' value L (step 2 of the design procedure), in this first optimization phase the impedance matching is considered the priority, and consequently, $\alpha = 0.6$ and $\beta = 0.4$.

Given the limited number of parameters to be optimized, the optimization has been carried out by analysing the behavior of each geometric variable with respect to the cost function Ψ. Towards this end, the value of the parameter under analysis has been varied while keeping the others to fixed values.

Fig. 2 shows the results of the parametric analysis on the main geometric variables. The total cost function Ψ is displayed in solid black, while the two components $\Psi_{S_{11}}$ and Ψ_{FB} are shown in dotted red and dashed red, respectively. The effect of varying the slot length s_l is shown in Fig. 2(a). As it can be noticed, a minimum of both the cost function terms, and consequently of the overall Ψ function, is obtained for $s_l = 56.5$ mm. As expected, such a value corresponds to about half a wavelength at f_c, as required by the slot to be resonant at the working frequency.

By varying the monopole height (Fig. 2(b)), the overall cost function Ψ is minimized for $m_h = 27$ mm. However, differently from the previous case, a variation of m_h affects only the $|S_{11}|$ term, while the Ψ_{FB} remains unchanged whatever the tested value. This can be ascribed to fact that the monopole height is mainly responsible for the variation of the impedance matching of the antenna, since it modifies the coupling with the slots.

As far as the cylinder height c_h is concerned, Fig. 2(c) clearly shows that a trade-off between the antenna impedance matching at the working frequency and FB has to be found. As a matter of fact, increasing the cylinder height improves the antenna FB, as shown by the decreasing Ψ_{FB} curve. However, because of the variation of the distance between the monopole and the slots, the impedance matching worsens. Moreover, it must be remembered that, as c_h increases, the overall antenna dimension increases as well, making the integration with IoT devices more complicated.

Finally, Fig. 2(d) shows that varying the horizontal distance s_d between two slots on the same level, an optimal value in terms of both $\Psi_{S_{11}}$ and Ψ_{FB} can be found. However, it must be pointed out that the effect of such a geometrical parameter on the antenna performance is much lower than that of s_l, m_h and c_h.

Finally, in order to obtain a compact antenna structure, the slot width (s_w) and the vertical gap between the two layers of slots (s_g) are required to be as small as possible (but allowing for an easy realization). Consequently, variations of a few millimeters, which correspond to small fractions of the wavelength in the 2.4 GHz band, have a very little effect on the antenna impedance matching and front-to-back ratio performance.

After the optimization process, the final values of the antenna geometric parameters result to be as follows: $\hat{\mathbf{a}} = \{s_l = 56.5, s_w = 3.0, s_g = 4.5, s_d = 18.83, c_h = 47.0, m_h = 27.0\}$ mm. The volume occupied by the antenna is therefore a cylinder of 72 mm diameter (0.59λ at f_c) and 47 mm height (0.38λ at f_c). The radius and the height of the cylindrical cavity are therefore 36 mm (0.29λ at f_c) and 47 (0.38λ at f_c)

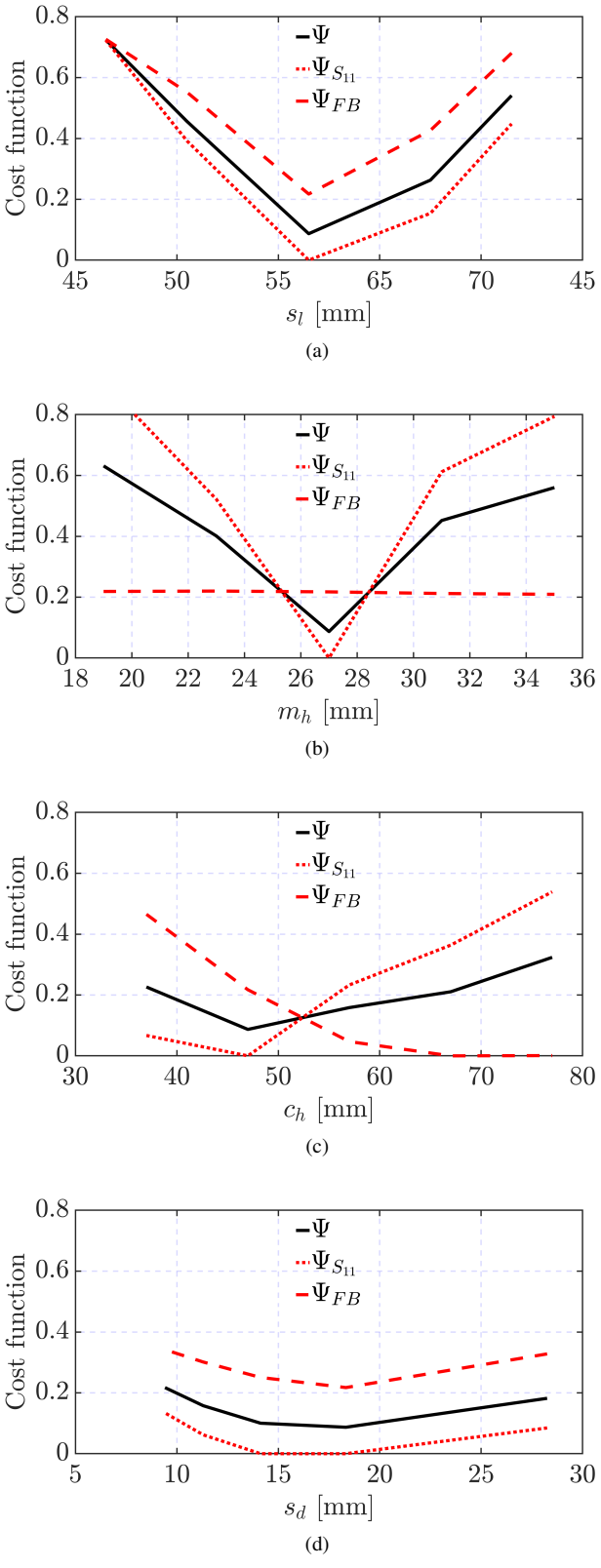

Figure 2. Optimization of the antenna geometrical parameters. Analysis of (a) the slot length s_l, (b) the monopole height m_h, (c) the cylinder height c_h, and (d) the distance between two adjacent slots on the same level s_d.

mm respectively. The total volume occupied by the antenna is 191.26 cm^3.

The second step of the antenna design procedure consists in the choice of the inductor to be placed in series to the switch on the slots. This inductor is used to further increase the overall FB of the antenna. This component, in fact, adds an additional degree of freedom to vary the radiating currents surrounding the slots and so to obtain the desired radiation behavior without modifying the antenna impedance matching. The resulting antenna characteristics for the different L values are summarized in Tab. I. The switch configuration is the same as for the antenna geometry optimization, i.e., all the switches are closed but the one on S_1. As it can be noticed, by varying the inductance value in the range $1.5 \leq L \leq 9.5$ nH, the FB can be increased up to 30 dB for $L = 3.9$ nH. In Tab. I, G_{max} indicates the gain in the direction of maximum radiation ($\varphi^{mr}, \theta = 90^o$), while G_{back} is the one at ($\varphi^{mr} - 180^o, \theta = 90^o$). It is worth noting that a good impedance matching with $|S_{11}|$ lower than -10 dB is maintained whatever the inductor value.

Table I
VARIATION OF THE MAIN ANTENNA CHARACTERISTICS FOR DIFFERENT VALUES OF THE INDUCTOR IN THE RECONFIGURATION CIRCUIT (FIG. 1).

L [nH]	$\|S_{11}\|$ [dB]	$G_{\max}$ [dBi]	G_{back} [dBi]	FB [dB]
1.5	-13.1	5.12	-10.81	15.93
2.3	-14.3	5.09	-14.05	19.14
3.1	-15.7	5.03	-19.05	24.08
3.9	-17.1	4.91	-25.78	30.69
4.7	-19.2	4.82	-24.93	29.75
5.5	-21.6	4.69	-17.83	22.52
6.3	-24.5	4.54	-14.15	18.69
7.1	-28.3	4.37	-11.74	16.11
7.9	-32.1	4.12	-10.01	14.13
8.7	-31.2	4.04	-8.07	12.11
9.5	-27.6	3.87	-7.66	11.52

C. Antenna Performance

The simulated performance of the final antenna structure (optimized geometry and $L = 3.9$ nH) are reported in the following.

The radiation pattern configurations that are provided by the antenna are shown in Fig. 3, where the total realized gain cuts in the horizontal plane are reported. Their main characteristics are summarized in Tab. II.

The first 6 configurations C_{1i}, $i = 1, ...6$ are obtained by sequentially reverse biasing each slot circuit, so that one switch at the time is open, while forward biasing all the others, so that they are closed. As it can be noticed, the patterns have a constant angular spacing of 60^o and they allow the 360^o coverage of the horizontal plane with a minimum gain between two consecutive patterns of 4.2 dBi. The realized gain in the direction of maximum radiation φ^{mr} is almost 5 dBi, while the half power beamwidth (HPBW) is about 110^o. Most importantly, the patterns exhibit a very high FB of more than 30 dB, which guarantees the filtering of the signals coming from the backward direction.

It must be pointed out that there are two main reasons for which it is important to use 6 pattern configurations to obtain the 360^o coverage.

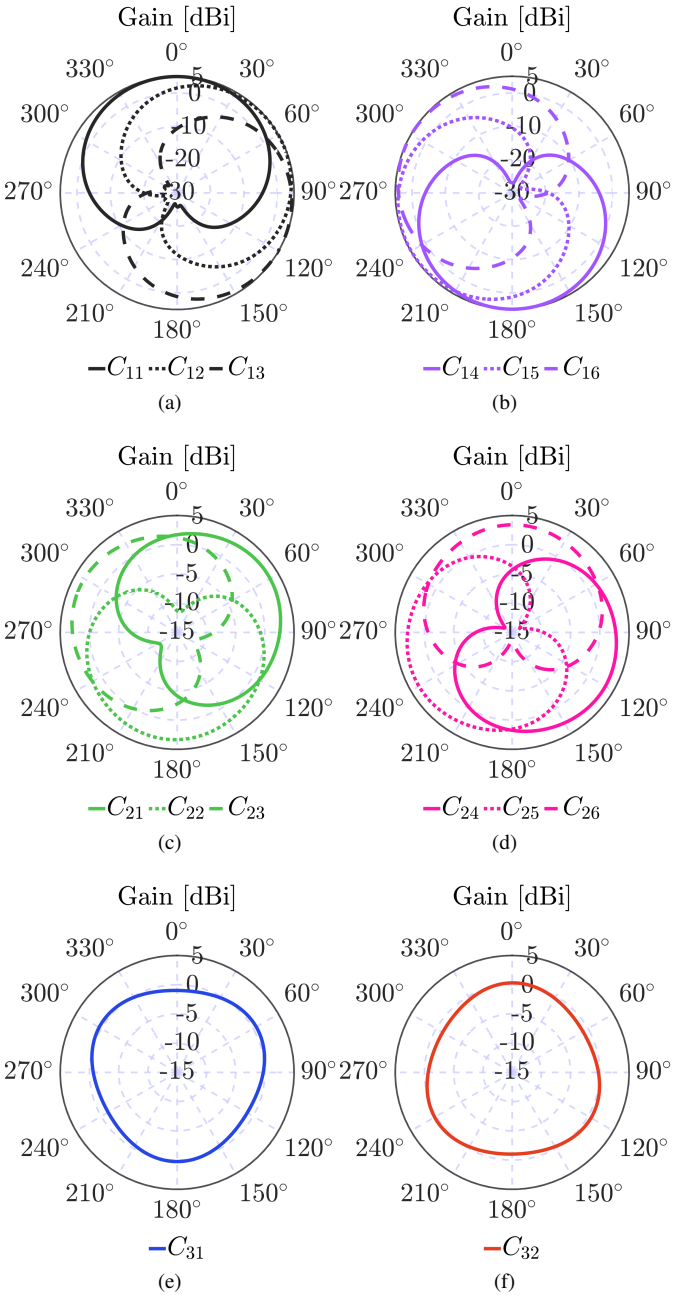

Figure 3. The different radiation pattern configurations provided by the antenna. The patterns represent the total realized gain in the azimuth plane.

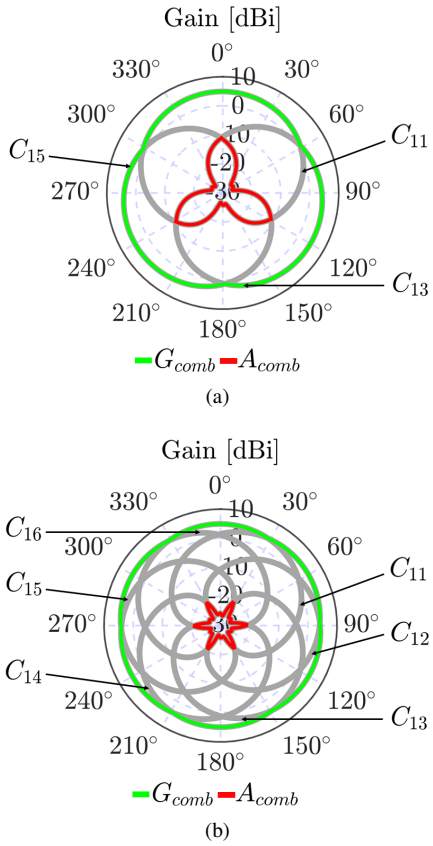

Figure 4. 360-degree coverage obtained considering (a) only 3 radiation states and (b) all the 6 radiation states $C_{11} - C_{16}$.

First, when less radiation states are considered (e.g., by selecting C_{11}, C_{13} and C_{15}), the 360^o coverage is obtained with a minimum gain of 1.24 dBi. This corresponds to the minimum between two consecutive patterns, as shown in Fig. 4(a), where the combined forward gain G_{CF} is highlighted in green. G_{CF} is obtained by selecting, for each azimuth direction, the highest gain value among the different antenna configurations. On the other hand, when all the 6 C_{1i} configurations are considered, the 360^o coverage is obtained with a minimum gain of 4.2 dBi (as shown in Fig. 4(b)). Such a difference (about 3 dB) is not negligible, since it increases the node communication distance or, alternatively, reduces the transmission power and consequently the node power consumption.

Secondly, and probably most importantly, using 6 radiation states allows a better spatial filtering accuracy. As shown in Fig. 4(b), the combined backward gain G_{CB}, defined as the lowest gain value among the different antenna configurations over the entire azimuth plane (highlighted in red) is always lower than -20 dBi. This guarantees a strong attenuation of the signals coming from the backward direction, and consequently less packet collisions and a lower average network power consumption (as demonstrated in [6]). When only 3 radiation patterns are used to obtain the 360^o coverage, G_{CB} can be as high as -10 dBi (Fig. 4(a)), which certainly reduces the level of the antenna filtering capability.

Configurations C_{2i}, $i = 1, ...6$ are obtained by simultaneously opening the switches of two consecutive slots located on the same level. The directions of maximum radiation are the same as in the previously discussed configurations. However, the resulting patterns exhibit a wider HPBW (about 160^o) with a slightly lower maximum gain (about 3.4 dBi). This allows the azimuth plane to be completely covered with a minimum gain of 2.8 dBi. The FB shown by $C_{21}...C_{26}$ decreases to about 15 dB. This is due to the fact that the FB optimization reported in Sect. II.B has been carried out on the reference configuration in which only one switch at a time was open.

Finally, by simultaneously opening 3 slots on the upper (S_1, S_3 and S_5) or lower level (S_2, S_4 and S_6), an omnidirectional behavior can be obtained. In both cases, the average gain is about -0.39 dBi with a maximum variation of 1.9 dB. This

Table II
MAIN CHARACTERISTICS OF THE DIFFERENT RADIATION PATTERN CONFIGURATIONS PROVIDED BY THE ANTENNA.

Conf.	Open switches	$\|S_{11}\|$ [dB]	$G_{\max}$ [dBi]	FB [dB]	$HPBW$ [deg]	φ^{mr} [deg]
C_{11} (dir)	W_1	-17.07	4.92	30.70	110.3	0
C_{12} (dir)	W_2	-15.21	4.89	31.79	108.8	60
C_{13} (dir)	W_3	-17.07	4.92	30.70	110.3	120
C_{14} (dir)	W_4	-15.21	4.89	31.79	108.8	180
C_{15} (dir)	W_5	-17.07	4.92	30.70	110.3	240
C_{16} (dir)	W_6	-15.21	4.89	31.79	108.8	300
C_{21} (dir)	$W_{1,3}$	-20.71	3.39	14.87	159.4	60
C_{22} (dir)	$W_{3,5}$	-20.71	3.39	14.87	159.4	180
C_{23} (dir)	$W_{5,1}$	-20.71	3.39	14.87	159.4	300
C_{24} (dir)	$W_{2,4}$	-18.76	3.41	15.74	160.6	120
C_{25} (dir)	$W_{4,6}$	-18.76	3.41	15.74	160.6	240
C_{26} (dir)	$W_{6,2}$	-18.76	3.41	15.74	160.6	0
C_{31} (omni)	$W_{1,3,5}$	-12.78	0.60	-	-	-
C_{32} (omni)	$W_{2,4,6}$	-12.77	0.57	-	-	-

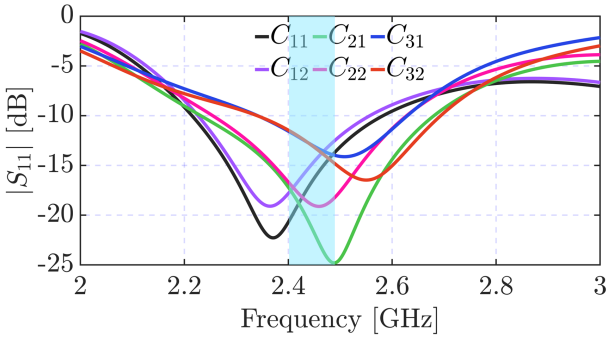

Figure 5. Reflection coefficient of the antenna in the different configurations.

mode is crucial in IoT applications since it allows network discovering procedures required during the deployment of the connected objects [6].

The antenna impedance matching in the different pattern configurations is shown in Fig. 5. Because of the circular symmetry of the antenna, only the results concerning the configurations C_{11}, C_{12}, C_{21}, C_{22}, and C_{31}, C_{32} are reported. As it can be seen, the antenna maintains a good matching ($|S_{11}| \leq -10$ dB) all over the the WiFi band ($2.40 - 2.48$ GHz), whatever the radiation pattern configuration.

III. IMPLEMENTATION

This section discusses the real implementation of the reconfiguration mechanism, that is, how the switches are realized, how they are electromagnetically modeled, and how the choice of the electronic components affects the performance of the antenna.

Figs. 6 and 7 present two different electronic implementations of the switches that have been tested. These configurations have been compared to the ideal one in which the two switch's states are modeled as perfect open and short circuits.

The first configuration I_1 (Fig.6(a)) is based on the use of one single PIN diode, which is DC biased through a choke inductor (L_{DC}) that prevents the RF current to flow to the ground on the polarization line. During the electromagnetic

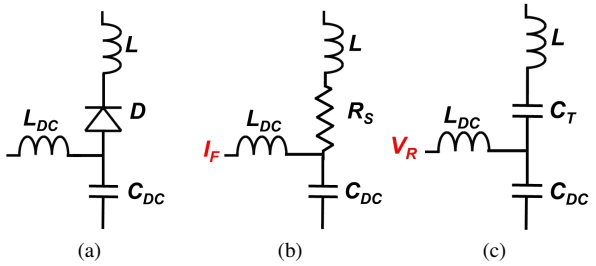

Figure 6. (a) Schematic of the one-diode electronic implementation I_1 of the reconfiguration mechanism. (b) Model of the circuit when forward biased with current I_F. (c) Model of the circuit when reverse biased with voltage V_R.

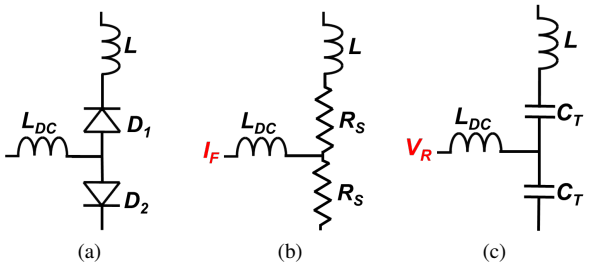

Figure 7. (a) Schematic of the two-diodes electronic implementation I_2 of the reconfiguration mechanism. (b) Model of the circuit when forward biased with current I_F. (c) Model of the circuit when reverse biased with voltage V_R.

Table III
MODEL PARAMETERS FOR THE 2 CONSIDERED DIODES.

DIODE	I_F	V_R	R_S	C_T	L_{DC}	L
SMP1345	0.5 mA	3.3 V	5 Ω	0.14 pF	100 nH	3.9 nH
SMP1322	0.5 mA	3.3 V	1.2 Ω	0.85 pF	100 nH	3.9 nH

simulations, two different models have been used for the open and closed switches. When forward biased (closed switch), the diode is modeled as a series resistance R_S accounting for the insertion losses of the component (Fig. 6(b)). The current flowing through the diode in the closed mode is indicated by I_F. When reverse biased with a voltage V_R (open switch), the diode is modeled as a capacitor C_T accounting for the parasitic coupling between the diode's terminals (Fig. 6(c)).

The second configuration I_2 is based on the use of two diodes connected as shown in Fig. 7(a) (common anode). This allows the total capacitance of the circuit in the open mode to be halved, since it is given by the series of the two diodes' equivalent capacitors (Fig. 7(c)). On the other hand, the overall resistance value of the circuit in the closed mode is therefore doubled (Fig. 7(b)). Moreover, this implementation avoids the use of the DC block C_{DC}, since it automatically prevents the short circuit of the DC polarization current. For each configuration, two different diodes from Skyworks (SMP1345 and SMP1322) are tested. The values of R_S and C_T as well as the required I_F and V_R used to control the two diodes are summarized in Tab. III.

To evaluate the impact on the antenna performance, the 4 implementations have been simulated in the C_{11} configuration

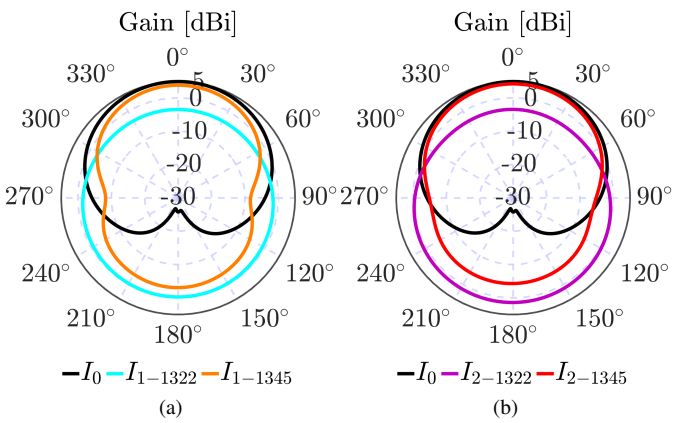

Figure 8. Comparison between the simulated realized gain patterns (azimuth plane) for the 4 different implementations of the reconfiguration mechanism and the pattern obtained in the ideal case (I_0).

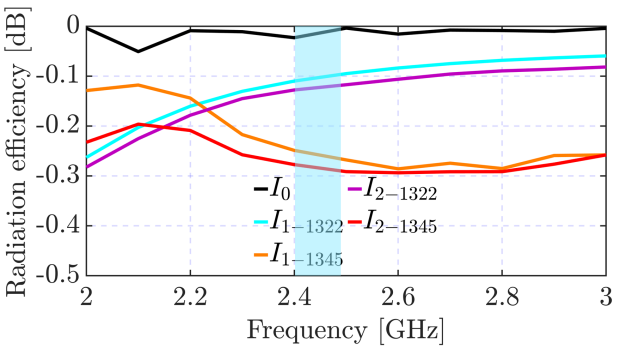

Figure 9. Simulated radiation efficiency obtained using the 4 different implementations of the reconfiguration mechanism.

and compared to the ideal case presented in Sect. II.C. Fig. 8 shows the comparison of the antenna radiation pattern obtained in the ideal case (I_0) with the those obtained using the 4 implementations. As it can be noticed, when the SMP1345 diode is used in the I_1 configuration (I_{1-1345}), the maximum gain in the desired direction (0^o) approaches the ideal value of 5 dBi. However, the FB is much lower (6.9 dB) than expected (30.7 dB). This can be ascribed to the 0.14 pF capacitance value modeling the diode when reverse biased, which limits the capacity of the diode to act as an open circuit. FB can be improved up to (8.5 dB) by adopting the two-diodes configuration (I_{2-1345}), in which the overall capacitance of the series of the two components is halved. Using higher-capacitance diodes, as the SMP1322 having $C_T = 0.85$ pF, results in much worse performance, whatever the considered implementation.

Low-capacitance diodes are, however, usually characterized by higher series resistances when forward biased, which will cause higher losses. In order to evaluate such a phenomenon, Fig. 9 shows the antenna radiation efficiency for the 4 implementations and the ideal case. As expected, in the I_1 implementation, the SMP1322 diode, characterized by 1.2Ω series resistance provides higher efficiency values than the SMP1345 one ($R_S = 5\Omega$) in the required frequency band. This behavior is even more visible in the I_2 mode, where the overall circuit resistance is doubled.

Nevertheless, for the proposed antenna geometry, the I_{2-1345} configuration seems to be the more suitable choice, since it allows the antenna to exhibit the best radiation performance (w.r.t. the ideal case), at the cost of a slight and acceptable efficiency reduction.

It is worth noticing that the practical implementation of the antenna, and consequently the choice of a specific commercially available electronic component has a strong impact on the antenna performance. These latter could be improved by a-priori selecting the commercial electronic components that will be used for the implementation and taking them into account during the antenna optimization phase.

IV. Numerical and Experimental Results

Based on the results shown in the previous section, the two-diodes implementation using the SMP1345 component (I_{2-1345}) has been selected. The numerical model of the antenna structure including the reconfiguration circuit is shown in Fig. 10. Differently from Fig. 1, the lateral surface of the cylinder is no more made of a simple copper sheet but it is realized by folding a thin double-sided flex PCB made from a polyimide film of 0.13 mm thickness and $\epsilon_r = 3.4$ dielectric permittivity. The inner side of the substrate is totally covered with metal except for the 6 slots. The external side is instead used as a support to print the metallic pads to place the electronic components (diodes and inductors) as well as the polarization lines of the reconfiguration circuit. These lines start at the bottom of the cylinder and proceed upwards to join the first pad used for the electronic components. Vias are used to create the electrical interconnection between the two sides of the PCB. The vias have a diameter of 0.48 mm. The prototype of antenna, in which the diodes and the inductors have been soldered, is shown in Fig. 11. On the bottom face of the cylinder, the prototype has been equipped with a classical SMA connector to feed the internal monopole and with 6 electrical wires soldered on the polarization lines to control the switches.

When the DC current is applied to one of the polarization lines (through the green wires in Fig. 11), the corresponding two diodes D_1 and D_2 are forward biased, so that the RF current can flow through them. Because of the vias connecting the inner and the outer metallic layer, the RF current path makes the slot to be shorted out.

To guarantee the robustness of the antenna in practical applications, the structural foam ROHACELL HF from Evonik has been placed inside the cylindrical cavity. The foam has been shaped in such a way as to completely fill the cylinder while leaving a central hole, along the entire height, for the insertion of the monopole. The foam has an extremely low relative permittivity ($\epsilon_r = 1.04$), which makes it electromagnetically transparent. The fine cell structure of the ROHACELL HF ensures minimal resin uptake, and problem-free compatibility with the inside metallic layer of the polyimide film that constitutes the lateral surface of the antenna, due to the absence of corrosive effects.

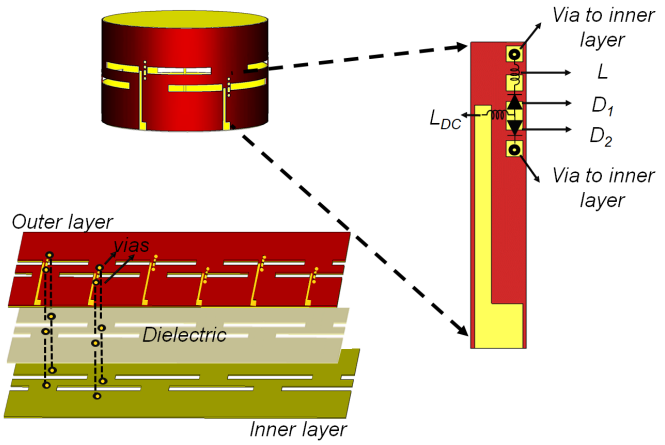

Figure 10. Numerical model of the antenna structure including the reconfiguration circuit implementation.

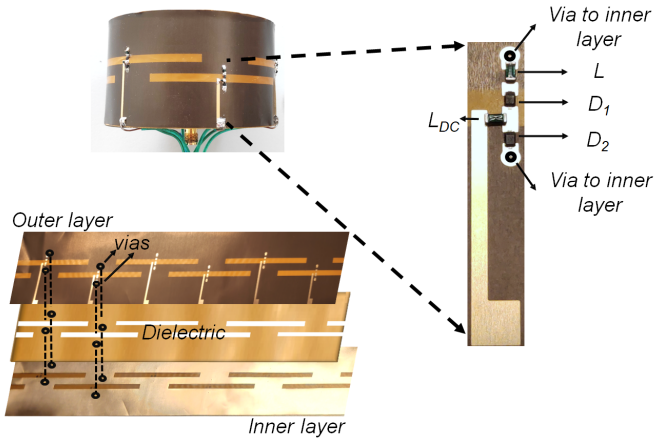

Figure 11. Antenna prototype.

Because of the symmetry of the antenna structure, only the experimental results of the configurations C_{11}, C_{21}, and C_{31} are reported. These configurations correspond to the cases where 1, 2 and 3 slots are open, respectively. Fig. 12 shows the comparison between simulated and measured $|S_{11}|$ for the three configurations. As it can be noticed, in all the cases the measured reflection coefficient is lower than -6 dB, which is acceptable for IoT applications. Since the reference configuration used for the antenna optimization (Sect. II) considered only one open slot, the best impedance matching is obtained for C_{11}. Nevertheless, acceptable results are obtained also for C_{21} and C_{31}. In general, a good agreement between simulations and measurements has been found, confirming the effectiveness of the numerical model in Fig. 10.

The measured realized total gain patterns in the horizontal and vertical planes are shown in Fig. 13. Whatever the considered configuration, a very good agreement with numerical data is visible. In configuration C_{11}, the maximum gain is about 4.29 dBi in the direction at 0^o and the main beam has a HPBW of 108^o. This latter allows the antenna to completely cover the horizontal plane with a minimum gain of 3.38 dBi when sequentially switching from C_{11} to C_{16}. The measured FB is 6.8 dB, making the antenna suitable for enabling spatial filtering. The side lobes appearing in the directions at $\theta = 0^o$ and $\theta = 180^o$ are caused by the presence of the top and bottom circular plates closing the cylindrical cavity. These metallic parts in fact contribute to the radiation of the antenna. However, it must be pointed out that, in IoT applications, the nodes are often supposed to be all located in the same horizontal plane. Concerning interference reduction, having a good FB in the horizontal plane ($\theta = 90^o$) is therefore more important than having side lobes in the vertical direction.

As for C_{21}, the maximum gain slightly decreases to 1.49 dBi while the HPBW increases to 165^o because of the effect of opening two consecutive slots. Finally, two omnidirectional radiation patterns are obtained in C_{31} and C_{32}. The maximum gain variation over the entire azimuth plane is less than 2.28 dB in simulations and 1.57 dB in measurements.

Finally, Fig. 14 shows the simulated and measured antenna total efficiency. Numerical values are higher than -1.5 dB all over the band of interest. As for the experimental data, the minimum total efficiencies are equal to -1.5 dB, -2 and -3 dB in the C_{11}, C_{21}, and C_{31} configurations, respectively. The differences between numerical and experimental data can be ascribed to imperfections in the realization of the prototype.

V. Conclusions

In this paper, a slot-based ESPAR antenna has been presented. Pattern reconfiguration is obtained by digitally controlling the states of PIN diodes located at the center of the slots in the structure. The antenna can provide 12 directive radiation patterns headed in 6 different directions and characterized by 2 different beamwidths as well as 2 omnidirectional patterns. The optimization of the antenna considering ideal components has been first presented and, successively, the practical implementation has been discussed. The importance of choosing low-capacitance PIN diodes to approach the ideal radiation behavior has been demonstrated. The effectiveness of the proposed solution has been experimentally validated. Thanks to its radiation properties (good FB, maximum of radiation in the horizontal plane, 360^o azimuth coverage) together with a compact and robust structure and a low-power and easy-to-control reconfiguration mechanism, the antenna is a perfect candidate to enable spatial filtering capabilities in crowded IoT wireless networks.

Thanks to its characteristics, the proposed antenna solution well fits the needs of large scale IoT networks. The antenna front-to-back ratio allows the antenna to focus the energy towards the desired communication direction and, most importantly, to spatially filter the signal coming from undesired directions, thus reducing the interference. This will cause the reduction of packet collisions and needed retransmissions, and therefore the node power consumption. The maximum of radiation in the azimuth plane maximizes the communication performance in the majority of IoT application scenarios (e.g., environment monitoring, automotive, smart city, etc.), in which the nodes of the networks are considered to be all located on the same horizontal plane. The 360° azimuth coverage, obtained by switching among the directive radiation configurations, allows the antenna to easily adapt to changes

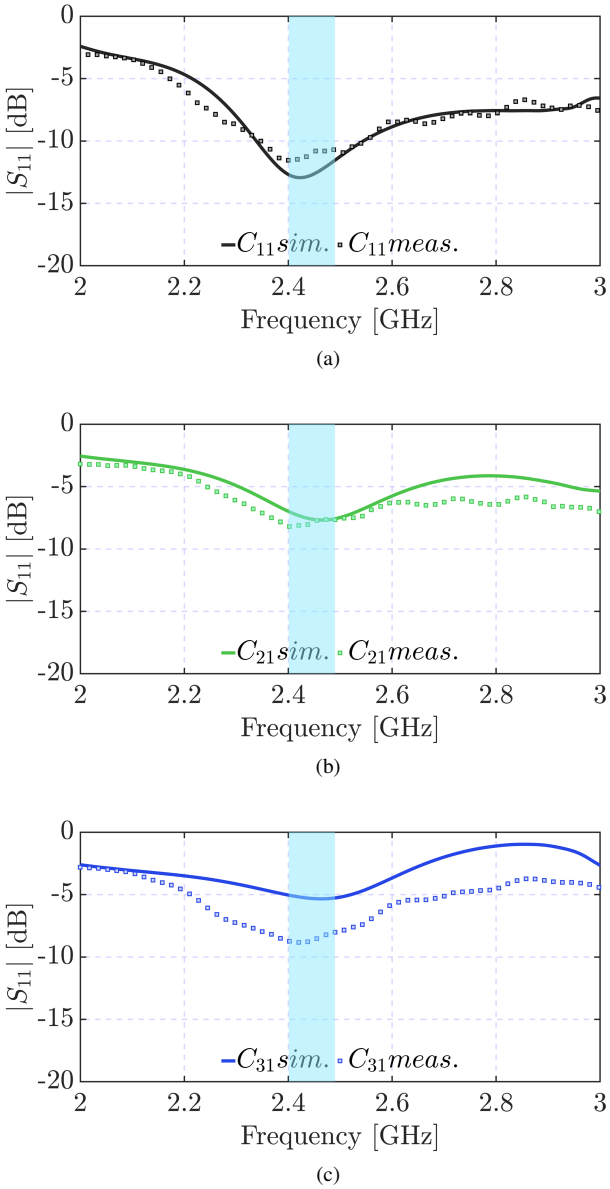

Figure 12. Simulated and measured impedance matching of the antenna in the different pattern configurations: (a) C_{11}, (b) C_{21} and (c) C_{31}.

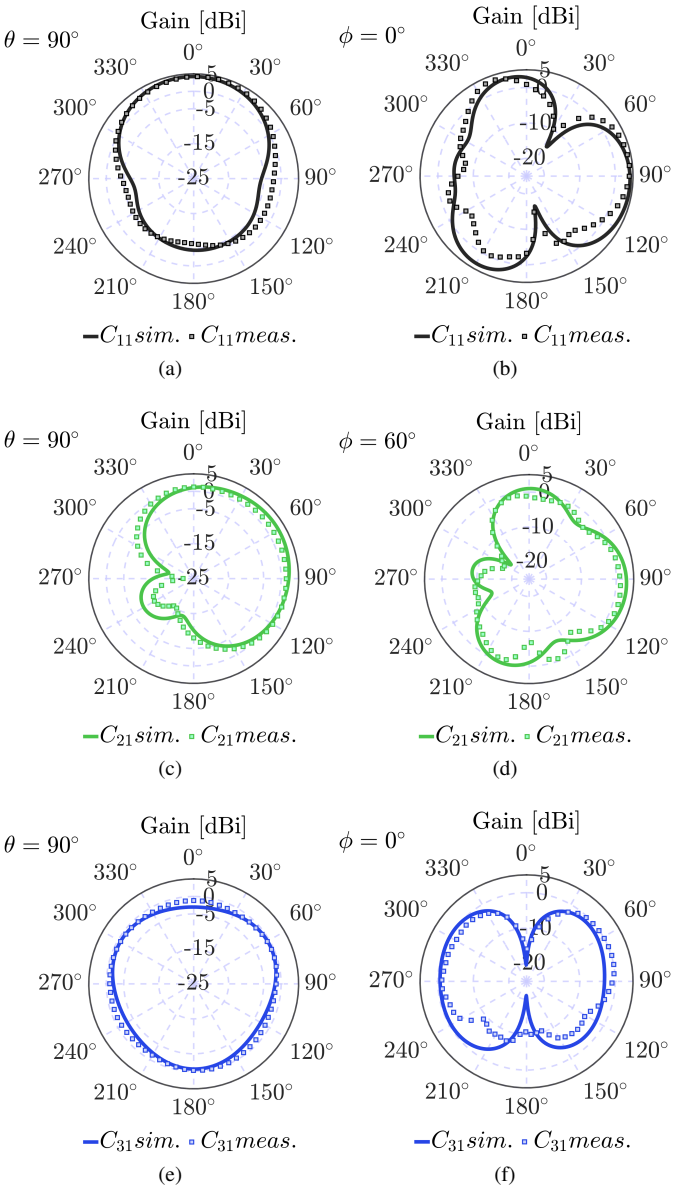

Figure 13. Simulated and measured realized gain patterns of the antenna in both (left) horizontal and (right) vertical planes for (a)-(b) C_{11}, (c)-(d) C_{21}, and (e)-(f) C_{31} pattern configurations.

in the network topology, while the available omnidirectional radiation behavior is important for specific IoT network setup processes, such as the node discovery. The compact and robust structure facilitates the integration with the IoT node electronics and the employment in harsh environments. Finally, the low-power (each diode consumes approximately 1.65 mW at 3.3 V) and easy-to-control reconfiguration mechanism (each slot can be activated using a simple digital output available on the IoT microcontroller) well fits the limited energy and computational resources usually available on autonomous IoT nodes.

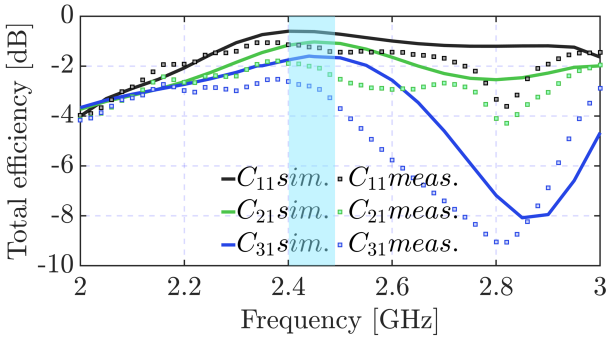

Figure 14. Simulated and measured antenna total efficiency in C_{11}, C_{21}, and C_{31} pattern configurations.

Acknowledgment

This work has been supported by the French government, through the UCA JEDI Investments in the Future project managed by the National Research Agency (ANR) with the

reference number ANR-15-IDEX-01. The author would like also to thank the CREMANT for its support in antenna measurements.

REFERENCES

[1] M. Frustaci, P. Pace, G. Aloi and G. Fortino, "Evaluating critical security issues of the IoT world: present and future challenges," *IEEE Internet of Things Journ.*, vol. 5, no. 4, pp. 2483-2495, 2018.

[2] N. Jiang, Y. Deng, A. Nallanathan, X. Kang and T. Q. S. Quek, "Analyzing random access collisions in massive IoT networks," *IEEE Trans. Wireless Comm.*, vol. 17, no. 10, pp. 6853-6870, 2018.

[3] X. Liu and N. Ansari, "Toward green IoT: energy solutions and key challenges," *IEEE Comm. Mag.*, vol. 57, no. 3, pp. 104-110, 2019.

[4] A. Paulraj, R. Nabar, and D. Gore, *Introduction to Space-Time Wireless Communications*, Cambridge University Press, 2003.

[5] W. Ouyang and X. Gong, "An electronically steerable parasitic array radiator (ESPAR) using cavity-backed slot antennas," *IEEE Antennas Wireless Propag. Lett.*, vol. 18, no. 4, pp. 757-761, 2019.

[6] T. N. Le, A. Pegatoquet, T. Le Huy, L. Lizzi, and F. Ferrero, "Improving energy efficiency of mobile wsn using reconfigurable directional antennas," *IEEE Communications Letters*, vol. 20, no. 6, pp. 1243-1246, 2016.

[7] R. Harrington, "Reactively controlled directive arrays," *IEEE Trans. Antennas Propag.*, vol. 26, no. 3, pp. 390-395, 1978.

[8] S. A. Mitilineos, K. S. Mougiakos and S. C. A. Thomopoulos, "Design and optimization of ESPAR antennas via impedance measurements and a genetic algorithm," *IEEE Antennas Propag. Mag.*, vol. 51, no. 2, pp. 118-123, 2009.

[9] O. Shibata and T. Furuhi, "Dual-band ESPAR antenna for wireless LAN applications" in *Proc. 2005 IEEE Antennas Propag. Soc. Int. Symp.*, Washington, DC, 2005, pp. 605-608 vol. 2B.

[10] Q. Wang and Z. Shen, "Modal expansion analysis of electrically steerable passive array radiator (ESPAR)," in *Proc. 2005 IEEE Antennas Propag. Soc. Int. Symp.*, Washington, DC, 2005, pp. 27-30 vol. 4B.

[11] H. Liu, S. Gao, and T. Loh, "Compact-size elecronically steerable parasitic array radiator antenna," in *Proc. 2009 Loughborough Antennas Propag. Conf.*, Loughborough, 2009, pp. 265-268.

[12] M. Burtowy, M. Rzymowski, and L. Kulas, "Low-profile ESPAR antenna for RSS-based DoA estimation in IoT applicaions," *IEEE Access*, vol. 7, pp. 17403-17411, 2019.

[13] H. Kawakami and T. Ohira, "Electrically steerable passive array radiator (ESPAR) antennas," *IEEE Antennas Propag. Mag.*, vol. 47, no. 2, pp. 43-49, 2005.

[14] J. Lu, D. Ireland, and R. Schlub, "Dielectric embedded ESPAR (DE-ESPAR) antenna array for wireless communications," *IEEE Trans. Antennas Propag.*, vol. 53, no. 8, pp. 2437-2443, 2005.

[15] R. Schlub and D. V. Thiel, "Switched parasitic antenna on a finite ground plane with conductive sleeve," *IEEE Trans. Antennas Propag.*, vol. 52, no. 5, pp. 1343-1347, 2004.

[16] H.-T. Liu, S. Gao, and T.-H. Loh, "Electrically small and low cost smart antennas for wireless communication," *IEEE Trans. Antennas Propag.*, vol. 60, no. 3, pp. 1540-1549, 2012.

[17] L. Batel, A. Clemente, and C. Delaveaud, "Superdirective and compact electronically-beam-switchable antenna for smart communication objects," in Proc. *2019 13th European Conference on Antennas and Propagation (EuCAP)*, Krakow, Poland, 2019, pp. 1-4.

[18] L. H. Trinh, T. N. Le, R. Staraj, F. Ferrero and L. Lizzi, "A Pattern-Reconfigurable Slot Antenna for IoT Network Concentrators," *Electronics*, vol. 6, no. 4, pp. 105-112, 2017.

[19] L. Santamaria, F. Ferrero and L. Lizzi, "Radiation pattern agile antenna for smart IoT gateways," in *Proc. of 2018 IEEE Int. Symp. Antennas Propag. & USNC/URSI Nat. Radio Science Meet.*, Boston, MA, 2018, pp. 977-978.

[20] T. Ohira and K. Gyoda, "Electronically steerable passive array radiator antennas for low-cost analog adaptive beamforming," in *Proc. 2000 IEEE Int. Conf. Phased Array Systems Techn. (Cat. No.00TH8510)*, Dana Point, CA, 2000, pp. 101-104.

[21] R. Schlub, Junwei Lu and T. Ohira, "Seven-element ground skirt monopole ESPAR antenna design from a genetic algorithm and the finite element method," *IEEE Trans. Antennas Propag.*, vol. 51, no. 11, pp. 3033-3039, 2003.